JPE 11-2-7

Oxidation Models of Rotor Bar and End Ring Segment to Simulate Induction Motor Faults in Progress

Jee-Hoon Jung†

† Smart Grid Research Division, Korea Electrotechnology Research Institute, Changwon, Korea

Abstract

Oxidation models of a rotor bar and end ring segment in an induction motor are presented to simulate the behavior of an induction machine working with oxidized rotor parts which are modeled as rotor faults in progress. The leakage inductance and resistance of the rotor parts are different from normal values because of the oxidation process. The impedance variations modify the current density and magnetic flux which pass through the oxidized parts. Consequently, it causes the rotor asymmetry which induces abnormal harmonics in the stator current spectra of the faulty machine. The leakage inductances of the oxidation models are derived by the Ampere's law. Using the proposed oxidation models, the rotor bar and end ring faults in progress can be modeled and simulated with the motor current signature analysis (MCSA). In addition, the oxidation process of the rotor bar and end ring segment can motivate the rotor asymmetry, which is induced by electromagnetic imbalances, and it is one of the major motor faults. Results of simulations and experiments are compared to each other to verify the accuracy of the proposed models. Experiments are achieved using 3.7 kW, 3-phase, and squirrel cage induction motors with a motor drive inverter.

Key Words: Fault diagnosis, Induction motor, Oxidation model, MCSA

NOMENCLATURE

V_s	Stator voltage vector (V)
V_r	Rotor voltage vector (V)
I_s	Stator current vector (A)
I_r	Rotor current vector (A)
Λ_s	Stator flux linkage vector (Wb)
Λ_r	Rotor flux linkage vector (Wb)
L_{ss}	Stator phase self-inductance matrix (H)
L_{rr}	Rotor loop self-inductance matrix (H)
L_{sr}	Mutual inductance matrix between stator phase and rotor loop (H)
T_{em}	Effective Electromagnetic motor torque (N·m)
J_m	Rotor inertia (kg·m^2)
θ_r	Rotor angular position (rad)
B_m	Viscous friction coefficient (kg/s)
T_L	Load torque (N·m)
l_r	Rotor axial length (m)
r_r	Distance from rotor center to the average length of air-gap (m)
μ_0	Permeability of air ($4\pi \times 10^{-7}$ H/m)
μ_{co}	Relative permeability of copper (0.99999)
$\mu_{co,o}$	Relative permeability of copper oxide (12)
σ_1	Conductivity of copper (5.80×10^7 S/m)
σ_2	Conductivity of copper oxide (4.71×10^2 S/m)
r	Distance from rotor bar center (m)
L_{hb}	Leakage inductance of healthy rotor bar (H)
L_{ob}	Leakage inductance of oxidized rotor bar (H)
R_{hb}	Resistance of healthy rotor bar (Ω)
R_{ob}	Resistance of healthy oxidized bar (Ω)
L_{he}	Leakage inductance of healthy end ring (H)
L_{oe}	Leakage inductance of oxidized end ring (H)
R_{he}	Resistance of healthy end ring (Ω)
R_{oe}	Resistance of oxidized end ring (Ω)

Manuscript received Jun. 18, 2010; revised Nov. 1, 2010
† Corresponding Author: jung.jeehoon@gmail.com
Tel: +82-55-510-1356, Mobile: +82-10-9811-3251, KERI
New & Renewable Energy System Research Center, Smart Grid Research Division, Korea Electrotechnology Research Institute, Korea

I. INTRODUCTION

Evidently, induction motors dominate the field of electromechanical power source, load, and energy conversion. Since several motors have been in charge of mechanical power sources for a main system, industrial applications have focused on the condition monitoring and fault diagnosis of motors to improve system stability and reliability. Therefore, an efficient maintenance method is necessity to utilize an induction machine in industrial applications. The condition-based maintenance (CBM) and noninvasive diagnosis of induction motors realized by on-line monitoring methods are focused on the most efficient way to maintain motors operating under healthy conditions [1]-[3].

Technical methods have been researched for the diagnosis and fault detection of an induction motor using various methodologies such as a vibration spectrum [4], model-based parameter tracking [5], power factor [6], and power signature analysis [7]. In addition, motor current signature analysis (MCSA) is one of the powerful noninvasive motor diagnosis methods to detect motor faults. It has several advantages such as no estimation of motor parameters, the simplicity of sensors, and their installation. Therefore, MCSA for incipient fault detection has received much attention in recent years [8], [9]. Many topics of MCSA have been researched to uplift its practical use in the industry field.

Simulation methods have been suggested to observe the spectrum of stator currents for each fault condition using mathematical models of faulty motors. Simulation model based on the finite element method was proposed to simulate a magnetic saturation caused by a rotor fault [10]. Electrical models of broken rotor parts for the rotor asymmetry have contributed to iterative computer simulations that extract the abnormal harmonics from stator currents [11], [12]. Several types of the air-gap eccentricity caused by the asymmetric motor structure or axis bending were modeled and simulated [13], [14]. Skewing and slot width effect (SWE) of rotor bars was considered to analyze practical induction motors which have complex rotor structures [15]. The simulations of induction motor faults were based on the winding function method (WFM) which accounts for space harmonics in electric machines [16].

New techniques have been developed for overcoming its weak points to use MCSA in a practical manner. Some researchers have developed motor diagnosis methods using MCSA with advanced signal processing techniques [17]-[19]. On-line condition monitoring of an induction motor was proposed to observe motor parameters such as the stator resistance and inductance [20]. Fault detection and classification methods have been developed based on MCSA [21]. In addition, MCSA has been improved by several estimation and optimization algorithms composed of advanced signal processing methods [22], [23]. Artificial intelligent algorithms such as the neural network have been also adopted to monitor the condition of induction machines [24]-[27]. They have successfully achieved the fault diagnosis of induction motors. However, there are no attempts or efforts to show the diagnostic possibility of motor faults in progress.

Several methods have been researched to detect partially broken rotor bar using the Hilbert Transform [28], starting current [29], and zero load and zero speed currents [30]. In addition, thermo-mechanical stresses experienced at the motor startup were introduced as a root cause of the rotor failure [31]-[33]. The expansion difference between the rotor bar and end ring caused by their temperature difference will fatigue their joint at the startup and cause rotor bar cracking and failures. Another root cause of the rotor failure is an oxidation process in rotor parts. Induction motors have been used under easily corrosive environments such as a submersible unprotected solid-rotor induction motor [34]. Corrosion can cause a rotor asymmetry as an environmental stress [35]. In addition, the oxidation is the first step of the thermal aging process in electrical machine when the motor is not running [32]. In this paper, oxidation models of a rotor bar and end ring segment are proposed to simulate the behavior of an induction machine containing abnormally oxidized rotor bars and end ring segments which are modeled as broken faults in progress.

The oxidation models have been suggested by [37], however, in this paper the models are expanded to the case of the fault in progress of the end ring segment. Model derivation, computer simulation using the proposed model, and physical experiment are newly achieved for the end ring segment. In addition, the slot width effect is newly considered to improve a model accuracy of the proposed method. They make the proposed model to be more elaborate by considering practical effects and faults of an end ring segment. The leakage inductances of oxidized parts are calculated from the relations among the magnetic energy, inductance, current, and magnetic flux density of stator and rotor windings by the Ampere's law. The leakage inductance and resistance of an oxidized rotor bar and end ring segment change during the oxidation process. Consequently, this partial variation of inductance and resistance causes the electromagnetic imbalance and rotor asymmetry. It also induces abnormal harmonics in the stator current spectra. The WFM is used to calculate the machine inductance, and the SWE of rotor bars is considered to develop more practical motor model. The simulations of the proposed oxidation models are presented to show the principle of the rotor asymmetry caused by the oxidation process, and experimental results validate the proposed erosion model using 3.7 kW, 3-phase, and squirrel cage induction motors with a motor drive inverter.

II. Dynamic Model of an Induction Motor

A. Electrical model of induction motor

Induction machine can be electrically modeled using the coupled magnetic circuit theory [16]. With assuming no motor loss and perfect insulation, the electrical model of an induction motor is based on voltage, current, and flux linkage equations with inductance and resistance matrices. Fig. 1 shows the electrical model of a 3-n winding induction motor. Electrical components of the motor model are composed of two parts: stator lines and rotor loops. Using the Kirchhoff's voltage and current laws, the voltage equations of the stator lines and rotor loops are described by the differential forms as follows:

$$V_s = R_s I_s + \frac{d\Lambda_s}{dt} \tag{1}$$

$$V_r = R_r I_r + \frac{d\Lambda_r}{dt}. \tag{2}$$

From flux relations between the stator and rotor windings, flux linkages of the stator and rotor are given by (3) and (4).

$$\Lambda_s = L_{ss} I_s + L_{sr} I_r \tag{3}$$

$$\Lambda_r = L_{rs} I_s + L_{rr} I_r. \tag{4}$$

The torque produced by rotating machine consists of the inertial torque, internal friction torque, and external load torque. The motor motion equation is derived as follows:

$$T_{em} = J_m \frac{d^2\theta_r}{dt^2} + B_m \frac{d\theta_r}{dt} + T_L = \frac{\partial W_{co}}{\partial \theta_r}. \tag{5}$$

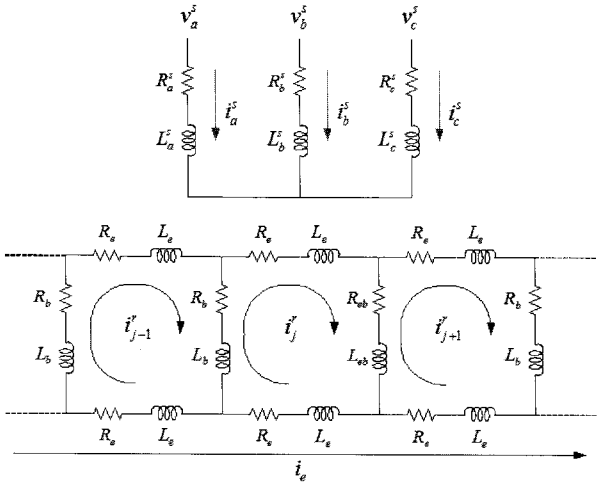

Fig. 1. Electrical model of a 3-n winding induction motor.

Assuming a linear magnetic system, the electrical motor torque can be obtained using the magnetic coenergy, W_{co}, which is the stored magnetic energy integrated by the magnetic flux λ according to the current i, as shown in (6) [25].

$$W_{co} = \int_0^i \lambda(i)\, di = \frac{1}{2} I^T L I. \tag{6}$$

For the convenience of calculation, suppose that B_m is small enough to ignore, then the rotor angular position, θ_r can be obtained from (5) and (6) as

$$\theta_r(t) = \frac{1}{J_m} \int_0^t \int_0^\tau \left[\frac{\partial}{\partial \theta_r} \left(\frac{1}{2} I^T L I \right) - T_L \right] dt d\tau \tag{7}$$

where τ is the internal time variable.

B. Winding function method (WFM)

The model based on the basic geometry and winding layout of an arbitrary n phase machine is suitable for time domain simulations of an AC machine. The WFM with the coupled magnetic circuit approach is a suitable model to analyze rotating machine including several types of faults [16]. The calculation of machine inductance is the key to a successful motor simulation. Fig. 2 shows the rotor slot structure which is the radial cross section of rotor parts. The angle of a slot opening width, ρ is obtained as follows:

$$\rho \approx \frac{2v}{r_r'} = \frac{2v}{r_r - v} \tag{8}$$

where r_r' is the distance between two centers of rotor and rotor bar, and v is the half width of a slot opening, respectively.

The mmf distribution, $F(\varphi, \theta)$ in the air-gap due to the current i can be calculated as follows:

$$F(\varphi, \theta) = N(\varphi, \theta) \cdot i \tag{9}$$

where $N(\varphi, \theta)$ is the modified winding function (MWF) defined as

$$N(\varphi, \theta) = n(\varphi, \theta) - \langle N(\theta) \rangle \tag{10}$$

$$\langle N(\theta) \rangle = \frac{1}{2\pi \langle g^{-1} \rangle} \int_0^{2\pi} n(\varphi, \theta) g^{-1}(\varphi, \theta) \cdot d\varphi \tag{11}$$

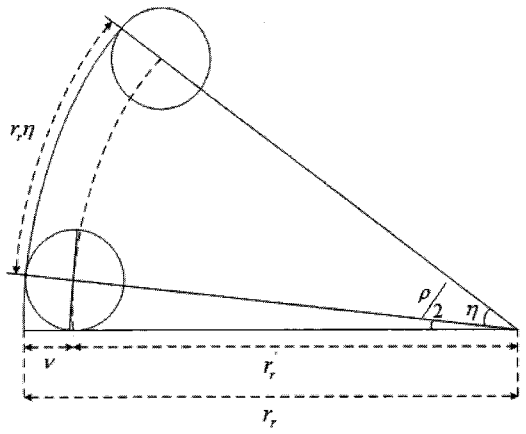

Fig. 2. Rotor slot structure.

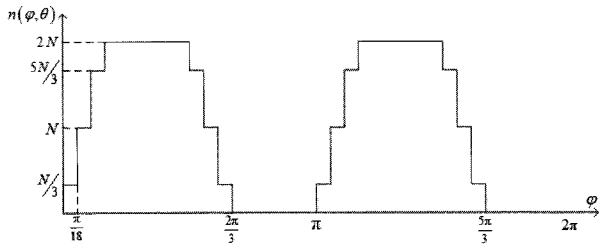

(a) Stator winding.

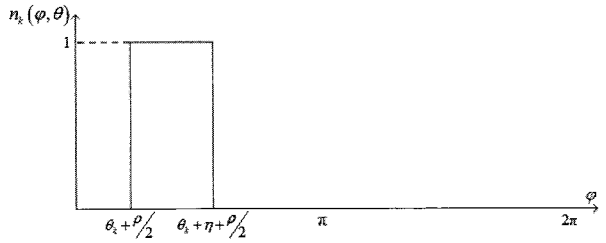

(b) Rotor bar.

Fig. 3. Winding distribution functions.

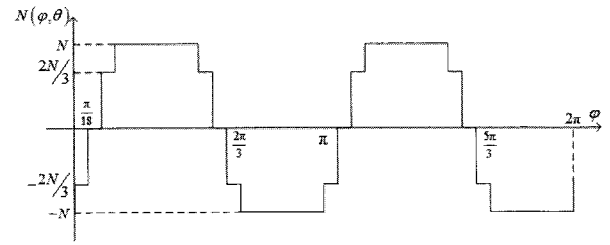

(a) Stator winding.

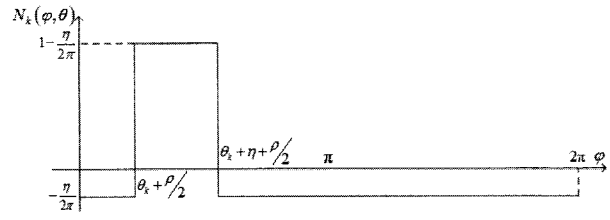

(b) Rotor bar.

Fig. 4. Modified winding functions.

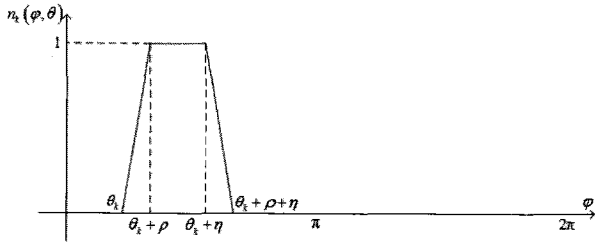

(a) Winding distribution function.

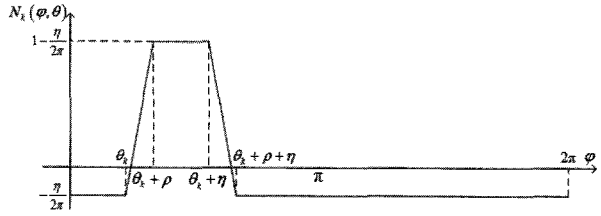

(b) Modified winding function.

Fig. 5. Rotor winding functions considering the SWE.

where $g(\varphi, \theta)$ is the air-gap function and $n(\varphi, \theta)$ is the turn function of a winding distribution according to the angle range φ and the angle position θ, respectively. Fig. 3 and 4 show the example graphs of the winding distribution function (WDF) and MWF of the stator winding and rotor bar, respectively. The magnetic flux, Φ is calculated as in (12).

$$\Phi(\theta) = \mu_0 r_r l_r \int_0^{2\pi} F(\varphi, \theta) g^{-1}(\varphi, \theta) d\varphi. \quad (12)$$

From (9) and (12), the inductance between the arbitrary coils i and j is given by (13).

$$L_{ij}(\theta) = \mu_0 r_r l_r \int_0^{2\pi} n_i(\varphi, \theta) N_j(\varphi, \theta) g^{-1}(\varphi, \theta) d\varphi. \quad (13)$$

C. Inductance calculation under slot width effect (SWE)

The machine inductances are calculated by the WDF and MWF. Using the SWE, the mmf functions are linearized across every rotor slots. Therefore, the WDF and MWF of the rotor bars are modeled as a ramp function instead of a step function across the rotor slots. Fig. 5 shows the WDF and MWF of the kth rotor bar considering the SWE. The analytical expressions of the WDF and MWF are derived as follows:

$$n_k(\varphi, \theta) = \begin{cases} \frac{\varphi - \theta_k}{\rho}, & \theta_k \le \varphi < \theta_k + \rho \\ 1, & \theta_k + \rho \le \varphi < \theta_k + \eta \\ \frac{\theta_k + \xi - \varphi}{\rho}, & \theta_k + \eta \le \varphi < \theta_k + \xi \\ 0, & \text{elsewhere} \end{cases} \quad (14)$$

$$N_k(\varphi, \theta) = n_k(\varphi, \theta) - \frac{\eta}{2\pi} \quad (15)$$

where η is the angle difference between two adjacent rotor slots, $\eta = 2\pi/Z$, Z is the number of rotor slots, and $\xi = \eta + \rho$, respectively. It is noted that the WDF and MWF have linear slopes within rotor slot opening regions.

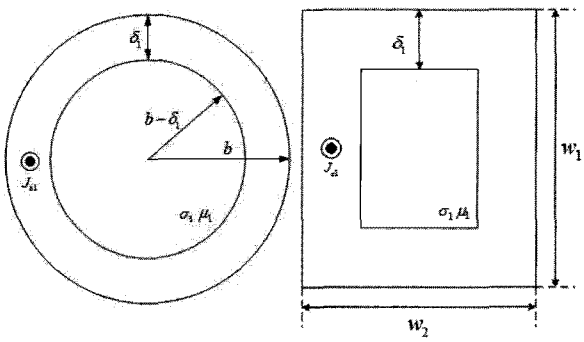

(a) Healthy rotor bar. (b) Healthy end ring segment.

Fig. 6. Cross sections of the healthy models.

III. Oxidation Models of Rotor Bar and End Ring Segment

A. Consideration of skin effect

Since the material of the rotor bar and end ring is copper, the shell of oxidation materials is made with a copper oxide. The rotor bar can generally be assumed as a cylindrical shape; therefore, its cross section can be regarded to a circle. Fig. 6 (a) shows the cross section of a healthy rotor bar with the skin depth of δ_1. In addition, the end ring has a toroidal shape, and its cross section is a rectangle. Fig. 6 (b) shows the cross section of a healthy end ring segment with parameters which are horizontal width, w_1, and vertical width, w_2.

The skin depths of the copper and copper oxide, δ_1 and δ_2, can be calculated as follows:

$$\delta_1 = \frac{1}{\sqrt{\pi f_{sl} \mu_1 \sigma_1}} = 2.17 \times 10^{-3} \text{m} \quad (16)$$

$$\delta_2 = \frac{1}{\sqrt{\pi f_{sl} \mu_2 \sigma_2}} = 6.85 \times 10^{-1} \text{m} \quad (17)$$

where the slip frequency, $f_{sl} = 0.4$ Hz in the steady state, $\mu_1 = \mu_{co}\mu_0$, and $\mu_2 = \mu_{co,o}\mu_0$, respectively.

B. Electromagnetic oxidation model of rotor bar

The current densities of the rotor bar's normal material (copper) part and oxidized material (copper oxide) part are assumed as J_{b1} and J_{b2}, respectively. By the Ampere's law, the magnetic flux density of the healthy rotor bar, B_{hb}, is calculated as

$$B_{hb} = \frac{r^2 - (b - \delta_1)^2}{2r} \mu_1 J_{b1} \quad (18)$$

where $b - \delta_1 \le r \le b$. As the same way, the magnetic flux density of the oxidized rotor bar, B_{ob}, is computed as

$$B_{ob} = \frac{\mu_2}{2r} \left[a^2 (J_{b1} - J_{b2}) + (b - \delta_3)^2 J_{b1} + r^2 J_{b2} \right] \quad (19)$$

where δ_3 is the skin depth of the oxidized rotor bar and $a \le r \le b$, respectively. Since the value of σ_2 is much smaller than σ_1, δ_3 can be obtained as shown in (20).

$$\delta_3 \approx b - a + \delta_1. \quad (20)$$

The currents of the healthy rotor bar, I_{hb}, and the oxidized rotor bar, I_{ob}, are calculated as follows:

$$I_{hb} = \pi \left(2b\delta_1 - \delta_1^2 \right) J_{b1} \quad (21)$$

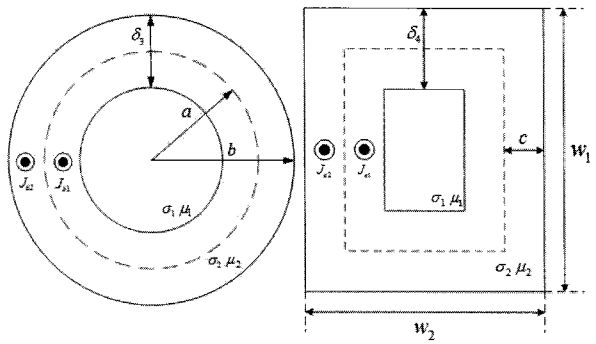

(a) Oxidized rotor bar. (b) Oxidized end ring segment.

Fig. 7. Cross sections of the oxidized models.

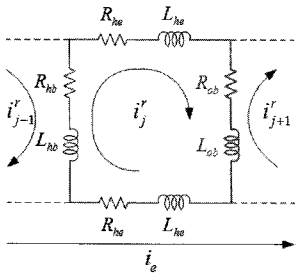

(a) Oxidized rotor bar model.

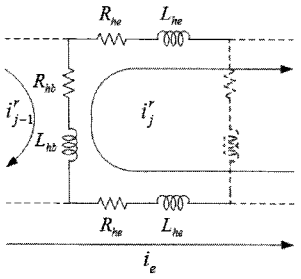

(b) Broken rotor bar model.

Fig. 8. Electrical circuit models of the rotor bars.

$$I_{ob} = \pi\left(a^2 - b^2\right)\left(J_{b1} - J_{b2}\right) + \pi\left(2b\delta_3 - \delta_3^2\right)J_{b1}. \tag{22}$$

Fig. 7 (a) shows the cross section of an oxidized rotor bar where the radius of the normal material part and entire rotor bar is a and b, respectively.

The relations of the magnetic energy, W, inductance, L, current, I, and magnetic flux density, B, can be described as

$$W = \frac{1}{2}LI^2 = \frac{1}{2}\int_V \frac{B^2}{\mu}dV \tag{23}$$

where V is the volume of the material. Using the magnetic leakage energy of the healthy and oxidized rotor bar, W_{hb}, W_{ob1}, and W_{ob2}, each leakage inductance can be calculated as follows:

$$L_{hb} = \frac{2W_b}{\left[\pi\left(2b\delta_1 - \delta_1^2\right)J_{b1}\right]^2} \tag{24}$$

$$L_{ob} = \frac{2\left(W_{ob1} + W_{ob2}\right)}{\pi^2\left[\left(a^2 - b^2\right)\left(J_{b1} - J_{b2}\right) + \left(2b\delta_3 - \delta_3^2\right)J_{b1}\right]^2} \tag{25}$$

where W_{hb}, W_{ob1}, and W_{ob2} can be calculated as follows:

$$W_{hb} = \frac{\mu_1\pi l_r}{4}J_{b1}^2\left[\left(b - \delta_{b1}\right)^4\left(\frac{3}{4} + \ln\frac{b}{b - \delta_{b1}}\right) - b^2\delta_{b1}^2 + \frac{b^4}{4}\right] \tag{26}$$

$$W_{ob1} = \frac{\mu_1\pi l_r}{4}J_{b1}^2\left[\delta_{a1}^4\left(\frac{3}{4} + \ln\frac{a}{\delta_{a1}}\right) - a^2\delta_{a1}^2 + \frac{a^4}{4}\right] \tag{27}$$

$$W_{ob2} = \frac{\mu_2\pi l_r}{4}\left\{\left(a^2J_{b12} - \delta_{b3}^2J_{b1}\right)^2 \cdot \ln\frac{b}{a} + \frac{b^4 - a^4}{4}J_{b2}^2 + \frac{b^2 - a^2}{2}\left(a^2J_{b2}J_{b12} - \delta_{b3}^2J_{b1}J_{b2}\right)\right\} \tag{28}$$

where $\delta_{a1} = a - \delta_1, \delta_{b1} = b - \delta_1$, $J_{b12} = J_{b1} - J_{b2}$, and $\delta_{b3} = b - \delta_1$, respectively.

The resistances of the healthy and oxidized rotor bar are obtained as shown in (29) and (30).

$$R_{hb} = \frac{l_r}{\pi\sigma_1\left(2b\delta_1 - \delta_1^2\right)} \tag{29}$$

$$R_{ob} = \frac{l_r}{\pi\sigma_1\left(2a\delta_1 - \delta_1^2\right) + \pi\sigma_2\left(2ba - a^2\right)}. \tag{30}$$

The variations of the rotor bar's leakage inductance and resistance, which are caused by the oxidation process, induce the rotor asymmetry which arouses abnormal harmonics in the stator current spectra. Fig. 8 (a) demonstrates the electrical circuit model with an oxidized rotor bar. The broken rotor bar in Fig. 8 (b) also causes rotor asymmetry. The broken bar does not participate in producing the electromagnetic force (emf) because the rotor bar current cannot pass through it. This difference makes the alternate degree of the rotor asymmetry between the oxidized and broken cases.

C. Electromagnetic oxidation model of end ring segment

The end ring's current densities of the normal and oxidized material parts are assumed as J_{e1} and J_{e2}, respectively. The shape of the end ring segment can be approximated to a rectangular cube illustrated in Fig. 9. Using the Ampere's law, the magnetic flux density of the healthy end ring segment, B_{he}, is calculated as follows:

$$B_{he} = \frac{\mu_1 J_{e1}}{x + y}\left[2xy - \frac{1}{2}\left(w_1 - 2\delta_1\right)\left(w_2 - 2\delta_1\right)\right] \tag{31}$$

where x is the horizontal distance and y is the vertical distance from the center of the end ring segment, which are limited to $w_1/2 - \delta_1 \le x \le w_1/2$ and $w_2/2 - \delta_1 \le y \le w_2/2$, respectively. As the same way, the magnetic flux density of the oxidized end ring segment, B_{oe}, is computed as

$$B_{oe} = \frac{\mu_2}{x + y}\left[J_{e1}\delta_{4c}w_\delta + J_{e2}\left(2xy - \frac{w_{c1}w_{c2}}{2}\right)\right] \tag{32}$$

where $\delta_{4c} = \delta_{4c} - c, w_\delta = w_1 + w_2 - 2(c + \delta_4)$, $w_{c1} = w_1 - 2c$, $w_{c2} = w_2 - 2c$ and x and y are limited to $w_1/2 - c \le x \le w_1/2$ and $w_2/2 - c \le y \le w_2/2$, respectively. Since δ_2 is small enough, the skin depth of δ_4 is obtained as shown in (33).

$$\delta_4 \approx c + \delta_1. \tag{33}$$

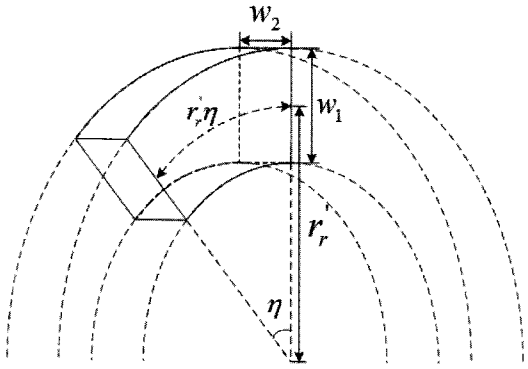

Fig. 9. Physical structure of the end ring segment.

The currents of the healthy and oxidized end ring segment, I_{he} and I_{oe}, are calculated as follows:

$$I_{he} = 2\delta_1 J_{e1}(w_1 + w_2 - 2\delta_1) \tag{34}$$

$$I_{oe} = 2(w_{c1} + w_2)(\delta_{4c} J_{e1} + cJ_{e2}) - 4\delta_4 J_{e1}\delta_{4c}. \tag{35}$$

Fig. 7 (b) shows the oxidized end ring segment with the depth of the oxidized material, c.

As the same way of the rotor bar case, the leakage inductance of the healthy and oxidized end ring segment can be calculated as

$$L_{he} = \frac{W_{he}}{2[\delta_1 J_{e1}(w_{\delta 1} + w_2)]^2} \tag{36}$$

$$L_{oe} = \frac{W_{oe1} + W_{oe2}}{2[(w_{c1} + w_2)(\delta_{4c} J_{e1} + cJ_{e2}) - 2\delta_{4c}\delta_4 J_{e1}]^2} \tag{37}$$

where the magnetic leakage energy of the healthy and oxidized end ring segment, W_{he}, W_{oe1}, and W_{oe2}, can be calculated as

$$W_{he} = \frac{4\pi r_r'}{Z}\mu_1 J_{e1}^2 \left[-2\alpha\delta_1^2 + f_1\left(\frac{w_1}{2}, \frac{w_{\delta 2}}{2}\right) + f_1\left(\frac{w_{\delta 1}}{2}, \frac{w_2}{2}\right) - f_1\left(\frac{w_1}{2}, \frac{w_2}{2}\right) - f_1\left(\frac{w_{\delta 1}}{2}, \frac{w_{\delta 2}}{2}\right) + g_1\left(\frac{w_1}{2}\right) - g_1\left(\frac{w_{\delta 1}}{2}\right)\right] \tag{38}$$

$$W_{oe1} = \frac{4\pi r_r'}{Z}\mu_1 J_{e1}^2 \left[-2\beta\delta_{4c}^3 + f_2\left(\frac{w_{c1}}{2}, \frac{w_{2\delta}}{2}\right) + f_2\left(\frac{w_{1\delta}}{2}, \frac{w_{c2}}{2}\right) - f_2\left(\frac{w_{c1}}{2}, \frac{w_{c2}}{2}\right) - f_2\left(\frac{w_{1\delta}}{2}, \frac{w_{2\delta}}{2}\right) + g_2\left(\frac{w_{c1}}{2}\right) - g_2\left(\frac{w_{1\delta}}{2}\right)\right] \tag{39}$$

$$W_{oe2} = \frac{4\pi r_r'}{Z}\mu_2 \left[-2\gamma c^2 J_{e2} + f_3\left(\frac{w_{c1}}{2}, \frac{w_2}{2}\right) + f_3\left(\frac{w_1}{2}, \frac{w_{c2}}{2}\right) - f_3\left(\frac{w_1}{2}, \frac{w_2}{2}\right) - f_3\left(\frac{w_{c1}}{2}, \frac{w_{c2}}{2}\right) + g_3\left(\frac{w_1}{2}\right) - g_3\left(\frac{w_{c1}}{2} - c\right)\right] \tag{40}$$

where $w_{\delta 1} = w_1 - 2\delta_1$, $w_{\delta 2} = w_2 - 2\delta_1$, $w_{1\delta} = w_1 - 2\delta_4$, $w_{2\delta} = w_2 - 2\delta_4$, and other functions and parameters can be obtained as follows:

$$f_1(m, n) = \kappa\left[2(m^4 + n^4) - \alpha(m^2 + n^2) + \frac{\alpha^2}{4}\right] \tag{41}$$

$$f_2(m, n) = \kappa\left[2(m^4 + n^4) - \beta(m^2 + n^2) + \frac{\beta^2}{4}\right] \tag{42}$$

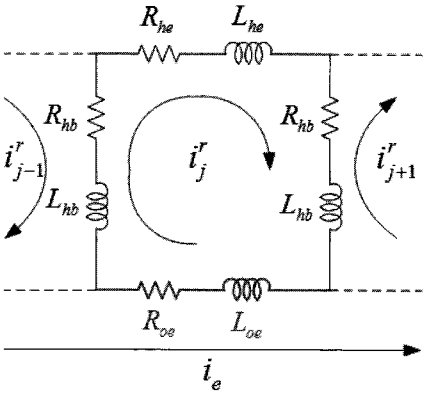

(a) Oxidized end ring segment model.

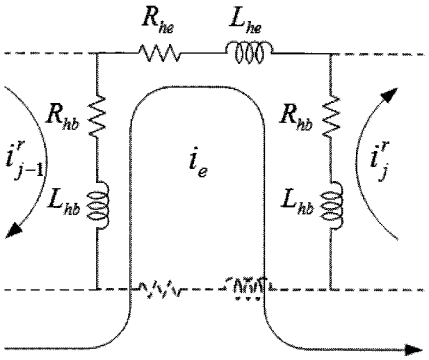

(b) Broken end ring segment model.

Fig. 10. Electrical circuit models of the end ring segments.

$$f_3(m, n) = \kappa\left[2J_{e2}^2(m^4 + n^4) - J_{e2}\gamma(m^2 + n^2) + \frac{\gamma^2}{4}\right] \tag{43}$$

$$\kappa = \ln(m + n) \tag{44}$$

$$\alpha = -w_{\delta 1} w_{\delta 2} \tag{45}$$

$$\beta = -w_{1\delta} w_{2\delta} \tag{46}$$

$$\gamma = 2J_{e1}\delta_{4c} w_\delta - J_{e2} w_{c1} w_{c2} \tag{47}$$

$$g_1(m) = \frac{m}{4}\left[w_2^3 - w_{\delta 2}^3 - m(w_2^2 - w_{\delta 2}^2) + 8m^2\delta_1\right] \tag{48}$$

$$g_2(m) = \frac{m}{4}\left[w_{c2}^3 - w_{2\delta}^3 - m(w_{c2}^2 - w_{2\delta}^2) + 8m^2\delta_{4c}\right] \tag{49}$$

$$g_3(m) = \frac{J_{e2}^2 m}{4}\left[w_2^3 - w_{c2}^3 - m(w_2^2 - w_{c2}^2) + 8m^2 c\right]. \tag{50}$$

The resistances of the healthy and oxidized end ring segment, R_{he} and R_{oe}, are calculated as follows:

$$R_{he} = \frac{r_r'\eta}{2\sigma_1\delta_1(w_{\delta 1} + w_2)} \tag{51}$$

$$R_{oe} = \frac{r_r'\eta}{2[\sigma_1\delta_{4c} w_\delta + \sigma_2 c(w_{c1} + w_2)]} \tag{52}$$

$$w_\delta = w_1 + w_2 - 2(c + \delta_4). \tag{53}$$

The variation of the leakage inductance and resistance of the end ring segment induces the rotor asymmetry in an electrical manner. This asymmetry significantly affects harmonic components in the stator current. Fig. 10 (a) demonstrates the electrical circuit model of the oxidized end ring segment. This

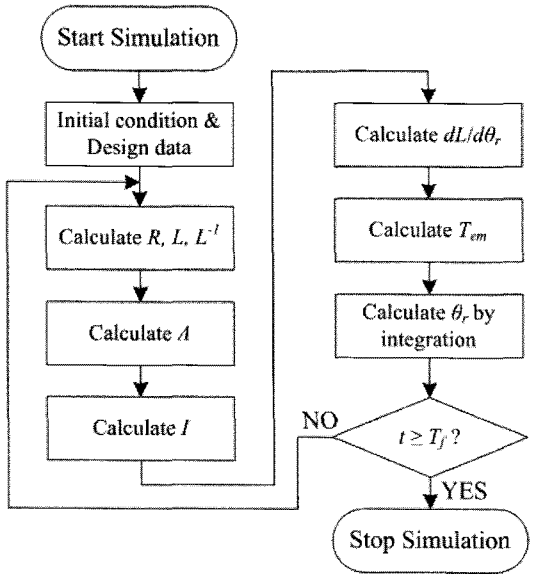

Fig. 11. Flowchart of simulation steps.

TABLE I
SPECIFICATION OF TARGET INDUCTION MOTOR

Specification	Value	Specification	Value
Rated Power	3.7 kW	# of Poles	4 EA
Input Voltage	220/380V	Input Current	13.8/8.0A
Frequency	60 Hz	Speed	1730rpm
Air-gap	4.56E-4m	Winding Type	Concentric
# of Stator Slot	36 EA	# of Rotor Bar	28 EA
Rotor Diameter	6.33E-2m	Core Length	1.02E-1m
Stator Resistance	1.53 Ω	Stator Inductance	2.73E-1H

oxidized part causes the rotor asymmetry. The broken case in Fig. 10 (b) also induces the rotor asymmetry. By the broken end ring segment, the end ring current is changed and its perturbation causes the electromagnetic asymmetry in the rotor structure. The difference of oxidized and broken faults, which is similar to the rotor bar case, makes the alternate degree of the rotor asymmetry between the oxidized and broken cases.

IV. RESULTS OF SIMULATION AND EXPERIMENT

In Table I, the specifications of the induction motor used in the simulation and experiment are shown. The stator winding has two pole pairs and wired with Y-connection. The spectral estimates of the stator current are the power spectral densities (PSDs) given by MATLAB function. Fig. 11 shows the flowchart of the proposed simulation step. Using this simulation sequence, the voltage and current waveforms of the target induction motor can be simulated with specific motor parameters. Fig. 12 (a) and (b) show a motor test bed and data acquisition interface used in the experiment, respectively. Stator current was measured using LabVIEW data acquisition software and NI6133 hardware interface developed by National Instrument.

In the oxidized rotor bar, J_{b2} is approximately $10^{-5}J_{b1}$ derived by the relations of σ_1 and σ_2. The radius of the normal part in the oxidized rotor bar is supposed as $a = 0.5b$. The radius of the total rotor bar is $b = 5$ mm, and the skin depths are $\delta_1 = 0.433b$ and $\delta_3 = 0.933b$. The relations of inductance and resistance are derived as $L_{ob} = 15.9L_{hb}$ and $R_{ob} = 2.65R_{hb}$. In the oxidized end ring segment, the current

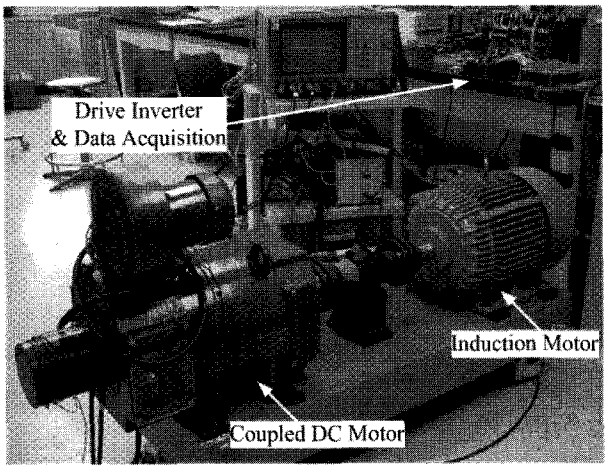

(a) Motor test bed.

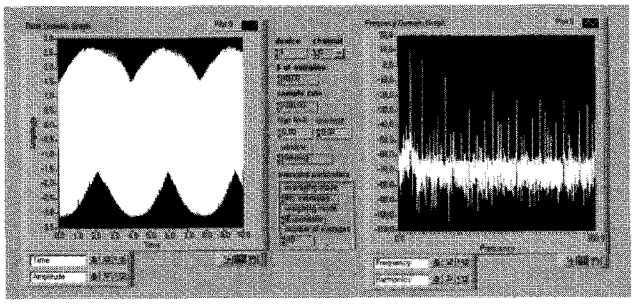

(b) Stator current data acquisition.

Fig. 12. Experimental setup and data acquisition.

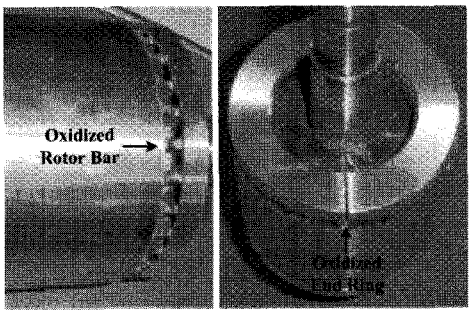

Fig. 13. Installation of the oxidized rotor bar and end ring segment.

density is $J_{e2} = 10^{-5}J_{e1}$. The depth of the oxidized material is $c = 0.150w_1$ and the widths are $w_1 = 18$ mm and $w_2 = 12$ mm. The skin depths are calculated as $\delta_1 = 0.145w_1$ and $\delta_4 = 0.295w_1$. The relations of the inductance and resistance are derived as $L_{oe} = 3.36L_e$ and $R_{ee} = 1.77R_e$, respectively. Fig. 13 shows the installation of the oxidized rotor bar and end ring segment in the induction motor for experiments. All the rotor bars and end rings used in the experiment were newly designed, produced, and inserted to the inside of the rotor frame by handwork. All the parameters of the prepared oxidized rotor bar and end ring segment used in the experiment are the same as the parameters explained above. The oxidized parts were made by a dielectric material which covered the outside of the normal material. The dielectric material was a mixture of oxidized materials which had similar electrical characteristics to the expected properties of the oxidized rotor bar and end ring segment.

Table II compares the parameter values among the healthy,

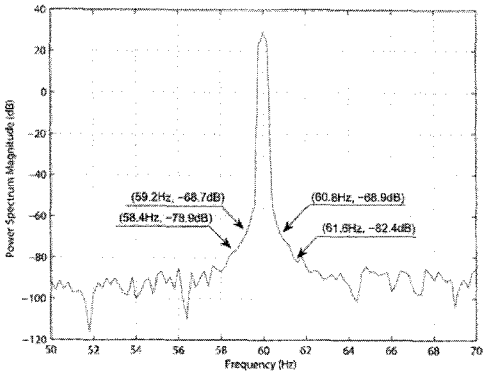

(a) Simulation result.

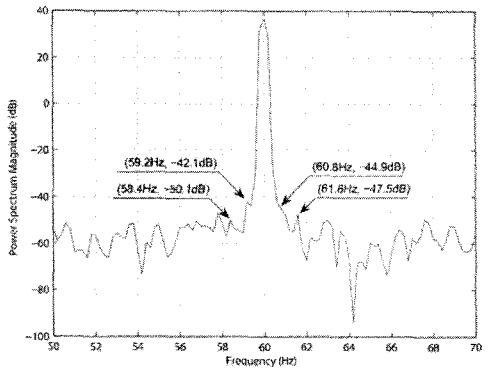

(b) Experimental result.

Fig. 14. Stator current spectra of the healthy rotor bar.

TABLE II
PARAMETER DIFFERENCES OF ROTOR BAR AND END RING

Parameter	Healthy	Oxidized	Broken
RB Resistance	6.28E-5Ω	1.66E-4Ω	∞
RB Leakage Inductance	2.21E-7H	3.51E-6H	∞
RB Magnetizing Inductance	1.54E-7H	1.54E-7H	3.08E-7H
ER Resistance	1.50E-6Ω	2.66E-6Ω	∞
ER Leakage Inductance	2.02E-8H	6.79E-8H	∞
ER Magnetizing Inductance	-	-	1.54E-7H

oxidized, and broken rotor bars and end ring segments. The resistance and leakage inductance of oxidized parts are larger than those of the healthy parts. The broken bar and segment reduce one current loop, and other loop currents make irregular torque pulsation and abnormal harmonics in stator current spectra. The proposed oxidation models are reasonable because the leakage inductance and resistance of the broken parts are infinite and those of the healthy parts are smaller than those of the oxidized part.

The abnormal harmonic frequencies of spectral components in the stator windings are given by [8]

$$f_{rotor} = (1 \pm 2ks) f_s \tag{54}$$

where f_s is the electrical supply frequency, s is the per unit (p.u.) slip, and k is the harmonic number as $k = 1,2,3,\ldots$, respectively. Fig. 14 to 18 show the power spectrum magnitudes of the stator current obtained by the simulation and experiment. The oxidized rotor bar and end ring segment used in the experiment were made by combining two different materials, copper and copper oxide, cylindrically. The load condition was a constant load set to 2 N·m. In addition, a spectral analysis was achieved using the power spectral density

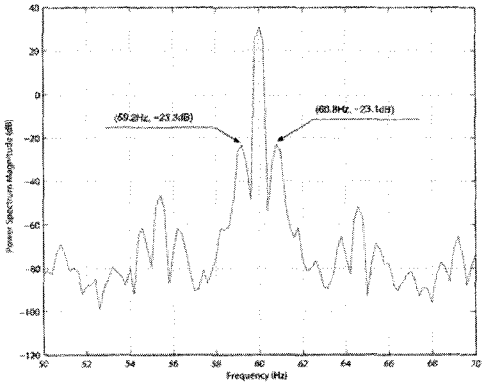

(a) Simulation result.

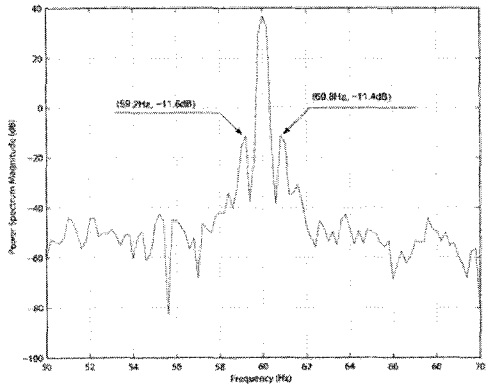

(b) Experimental result.

Fig. 15. Stator current spectra of the oxidized rotor bar.

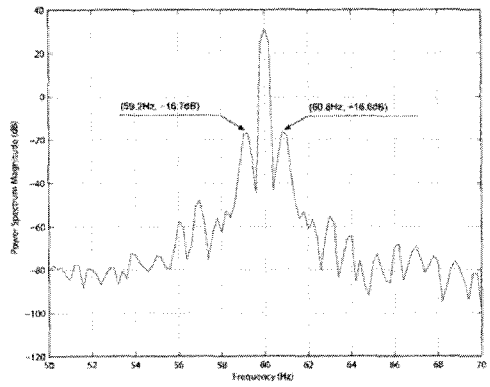

(a) Simulation result.

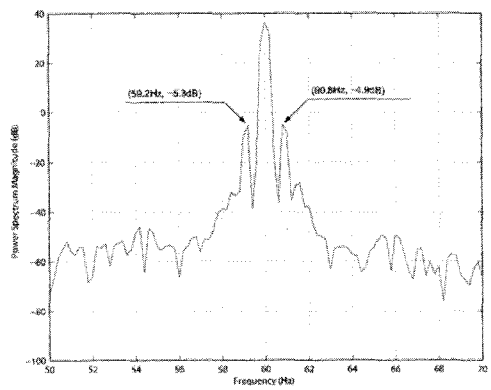

(b) Experimental result.

Fig. 16. Stator current spectra of the broken rotor bar.

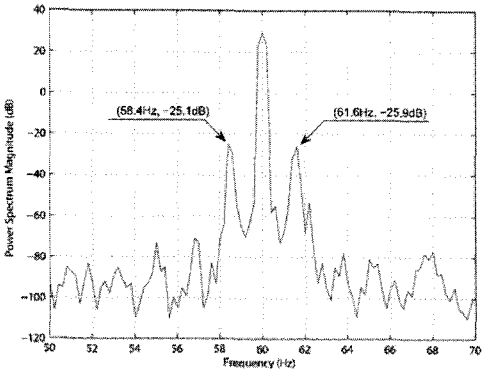

(a) Simulation result.

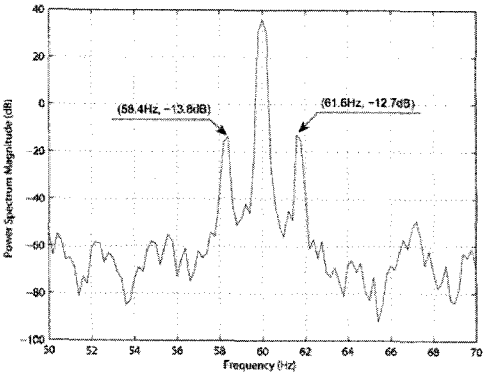

(b) Experimental result.

Fig. 17. Stator current spectra of the oxidized end ring segment.

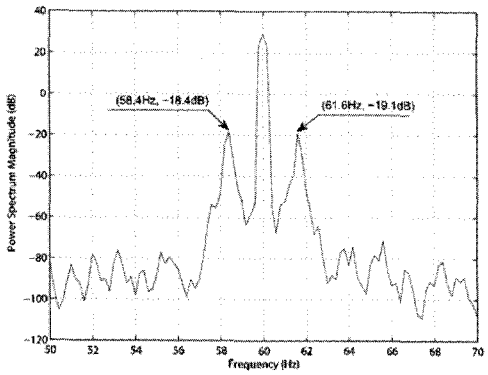

(a) Simulation result.

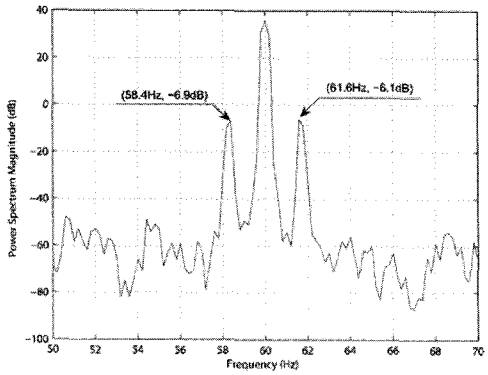

(b) Experimental result.

Fig. 18. Stator current spectra of the broken end ring segment.

TABLE III
SPECTRUM MAGNITUDES OF SIMULATION AND EXPERIMENT

Spectrum Magnitude	Simulation (dB)		Experiment (dB)	
	Left	Right	Left	Right
Healthy Rotor Bar	-68.7	-68.9	-42.1	-44.9
Oxidized Rotor Bar	-23.3	-23.1	-11.6	-11.4
Broken Rotor Bar	-16.7	-16.6	-5.3	-4.9
Healthy End Ring	-78.9	-82.4	-50.1	-47.5
Oxidized End Ring	-25.1	-25.9	-13.8	-12.7
Broken End Ring	-18.4	-19.1	-6.9	-6.1

normalized to a dc value of the stator current spectrum. All cases have a 0.4 Hz slip frequency with the constant load.

From (54), abnormal harmonic frequencies of the stator current in the cases of the oxidized and broken rotor bar faults are obtained as 59.2 Hz and 60.8 Hz with the harmonic number, $k = 1$, respectively. In addition, the frequency of 58.4 Hz and 61.6 Hz are detected as the abnormal harmonics in the case of end ring failures with $k = 2$. Table III shows the spectrum magnitudes of the abnormal harmonics obtained by the simulation and experiment. Obviously, the power spectrum magnitudes of the rotor bar and end ring faults have a tendency that the power spectrum magnitudes of the oxidized part have a position between the cases of the healthy and broken parts. In addition, this tendency appears in both of simulated and experimental results. Consequently, the proposed oxidation models can successfully simulate a case of rotor bar and end ring faults in progress and demonstrate rotor fault sequences before the rotor parts are broken.

V. CONCLUSION

The oxidation models of the rotor bar and end ring faults in progress are proposed to simulate the behavior of the induction motors working with rotor faults. The oxidation models are derived using the Ampere's law; in addition, the WFM is used for the calculation of a machine inductance. The SWE is also considered to establish the elaborate model of an induction motor. The variations of the leakage inductance and resistance in the oxidized parts cause the rotor asymmetry which makes the abnormal harmonics in the stator current spectra. From the simulated and experimental results of the spectral analysis for the oxidation models, the spectrum magnitudes of the erosive rotor bar and end ring segment have a position between the spectrum magnitudes of the healthy and broken case. Therefore, the proposed oxidation models are reasonable to understand the characteristics of the rotor bar and end ring faults in progress. In addition, they successfully simulate the operation of the induction motors containing not only broken rotor parts but also rotor faults in progress.

REFERENCES

[1] M. E. H. Benbouzid, "A review of induction motors signature analysis as a medium for faults detection," *IEEE Trans. Ind. Eletron.*, Vol. 47, No. 5, pp. 984-993, Oct. 2000.

[2] M. A. Awadallah and M. M. Morcos, "Application of AI tools in fault diagnosis of electrical machines and drives-an overview," *IEEE Trans. Energy Conv.*, Vol. 18, No. 2, pp. 243-251, Jun. 2003.

[3] R. M. Tallam, S. B. Lee, G. C. Stone, G. B. Kliman, J. Yoo, T. G. Habetler, and R. G. Harley, "A survey of methods for detection of stator-related faults in induction machines," *IEEE Trans. Ind. Appl.*, Vol. 43, No. 4, pp. 920-933, Jul./Aug. 2007.

[4] A. Sadoughi, M. Ebrahimi, M. Moallem, and S. Sadri, "Intelligent diagnosis of broken bars in induction motors based on new features in vibration spectrum," *Journal of Power Electronics*, Vol. 8, No. 3, pp. 228-238, Jul. 2008.
[5] C. Kral, F. Pirker, G. Pascoli, and H. Kapeller, "Robust rotor fault detection by means of the vienna monitoring method and a parameter tracking technique," *IEEE Trans. Ind. Electron.*, Vol. 55, No. 12, pp. 4229-4237, Dec. 2008.
[6] A. Ibrahim, M. El Badaoui, F. Guillet, and F. Bonnardot, "A new bearing fault detection method in induction machines based on instantaneous power factor," *IEEE Trans. Ind. Electron.*, Vol. 55, No. 12, pp. 4252-4259, Dec. 2008.
[7] M. Drif and A. J. M. Cardoso, "The use of the instantaneous-reactive-power signature analysis for rotor-cage-fault diagnostics in three-phase induction motors," *IEEE Trans. Ind. Electron.*, Vol. 56, No. 11, pp. 4606-4614, Nov. 2009.
[8] W. T. Thomson and M. Fenger, "Current signature analysis to detect induction motor faults," *IEEE-Industry Applications Magazine*, Vol. 7, No. 4, pp. 26-34, Jul./Aug. 2001.
[9] M.E.H. Benbouzid and G.B. Kliman, "What stator current processing-based technique to use for induction motor rotor faults diagnosis?," *IEEE Trans. Energy Convers.*, Vol. 18, No. 2, pp. 238-244, Jun. 2003.
[10] J. Sprooten and J.-C. Maun, "Influence of saturation level on the effect of broken bars in induction motors using fundamental electromagnetic laws and finite element simulations," *IEEE Trans. Energy Convers.*, Vol. 24, No. 3, pp. 557-564, Sep. 2009.
[11] H. A. Toliyat, and T. A. Lipo, "Transient analysis of cage induction machines under stator, rotor bar and end ring faults," *IEEE Trans. Energy Convers.*, Vol. 10, No. 2, pp. 241-247, Jun. 1995.
[12] N.-H. Kim, W.-S. Baik, M.-H. Kim, and C.-H. Choi, "Rotor fault detection system for the inverter driven induction motor using current signals," *Journal of Power Electronics*, Vol. 9, No. 2, pp. 224-231, Mar. 2009.
[13] N.-T. Nguyen and H.-H. Lee, "Decision tree with optimal feature selection for bearing fault detection," *Journal of Power Electronics*, Vol. 8, No. 1, pp. 101-107, Jan. 2008.
[14] J. Faiz, B. M. Ebrahimi, B. Akin, and H. A. Toliyat, "Dynamic analysis of mixed eccentricity signatures at various operating points and scrutiny of related indices for induction motors," *IET Elec. Power Appl.*, Vol. 4, No. 1, pp. 1-16, Jan. 2010.
[15] G. M. Joksimovic, M. D. Durovic, and A. B. Obradovic, "Skew and linear rise of MMF across slot modeling - Winding function approach," *IEEE Trans. Energy Convers.*, Vol. 14, No. 3, pp. 315–320, Sep. 1999.
[16] X. Luo, Y. Liao, H. A. Toliyat, A. El-Antably, and T. A. Lipo, "Multiple coupled circuit modeling of induction machines," *IEEE Trans. Ind. Appl.*, Vol. 31, No. 2, pp. 311-318, Mar./Apr. 1995.
[17] N. H. Kim, "Rotor fault detection system for inverter driven induction motors using currents signals and an encoder," *Journal of Power Electronics*, Vol. 7, No. 4, pp. 271-277, Oct. 2007.
[18] J. Cusido, L. Romeral, J. A. Ortega, J. A. Rosero, and A. Garcia Espinosa, "Fault detection in induction machines using power spectral density in wavelet decomposition," *IEEE Trans. Ind. Electron.*, Vol. 55, No. 2, pp. 633-643, Feb. 2008.
[19] S. H. Kia, H. Henao, and G.-A. Capolino, "Diagnosis of broken-bar fault in induction machines using discrete wavelet transform without slip estimation," *IEEE Trans. Ind. Appl.*, Vol. 45, No. 4, pp. 1395-1404, Jul./Aug. 2009.
[20] C. H. De Angelo, G. R. Bossio, S. J. Giaccone, and M. I. Valla, "Online model-based stator-fault detection and identification in induction motors," *IEEE Trans. Ind. Electron.*, Vol. 56, No. 11, pp. 4671-4680, Nov. 2009.
[21] J. Yun, K. Lee, K.-W. Lee, S. B. Lee, and J.-Y. Yoo, "Detection and classification of stator turn faults and high-resistance electrical connections for induction machines," *IEEE Trans. Ind. Appl.*, Vol. 45, No. 2, pp. 666-675, Mar./Apr. 2009.
[22] J. H. Jung, J. J. Lee, and B. H. Kown, "Online diagnosis of induction motors using MCSA," *IEEE Trans. Ind. Electron.*, Vol. 53, No. 6, pp. 1842-1852, Dec. 2006.
[23] S.H. Kia, H. Henao, and G.-A. Capolino, "A high-resolution frequency estimation method for three-phase induction machine fault detection," *IEEE Trans. Ind. Eletron.*, Vol. 54, No. 4, pp. 2305-2314, Aug. 2007.
[24] M. Moradian, M. Ebrahimi, M. Danesh, and M. bayat, "Detection of broken bars in induction motors using a neural network," *Journal of Power Electronics*, Vol. 6, No. 4, pp. 245-252, Jul. 2006.
[25] M. S. Ballal, H. M. Suryawanshi, and M. K. Mishra, "Detection of incipient faults in induction motors using FIS, ANN and ANFIS techniques," *Journal of Power Electronics*, Vol. 8, No. 2, pp. 181-191, Apr. 2008.
[26] F. Zidani, D. Diallo, M. E. H. Benbouzid, and R. Nait-Said, "A fuzzy-based approach for the diagnosis of fault modes in a voltage-fed PWM inverter induction motor drive," *IEEE Trans. Ind. Electron.*, Vol. 55, No. 2, pp. 586-593, Feb. 2008.
[27] M. Bouzid, G. Champenois, N. M. Bellaaj, L. Signac, and K. Jelassi, "An effective neural approach for the automatic location of stator interturn faults in induction motor," *IEEE Trans. Ind. Electron.*, Vol. 55, No. 12, pp. 4277-4289, Dec. 2008.
[28] G. Didier, E. Ternisien, O. Caspary, and H. Razik, "A new approach to detect broken rotor bars in induction machines by current spectrum analysis," *Mechanical Systems and Signal Processing*, Vol. 21, No. 2, pp. 1127-1142, Feb. 2007.
[29] R. Supangat, N. Ertugrul, W. L. Soong, D. A. Gray, C. Hansen, and J. Grieger, "Detection of broken rotor bars in induction motor using starting-current analysis and effects of loading," *IEE Proc. Electric Power Applications*, Vol. 153, No. 6, pp. 848-855, Nov. 2006.
[30] T. M. Wolbank, P. Nussbaumer, H. Chen, P. E. Macheiner, "Monitoring of rotor bar defects in inverter-fed induction machines at zero load and speed," to appear in *IEEE Trans. Ind. Electron.*
[31] I. D. Lomax, "Assessment of induction motor cage fatigue life," *5th Int. Conf. Electrical Machines and Drives*, pp. 281-284, 1991.
[32] T. Albers and A. H. Bonnett, "Motor temperature considerations for pulp and paper mill applications," *IEEE Trans. Ind. Appl.*, Vol. 38, No. 6, pp. 1701-1713, Nov./Dec. 2002.
[33] G. Donner, B. K. Oakes, and S. T. Evon, "Motor primer—Part III," *IEEE Trans. Ind. Appl.*, Vol. 39, No. 5, pp. 1467-1474, Sep./Oct. 2003.
[34] J. B. Danilevich, V. N. Antipov, I. Y. Kruchinina, and Y. P. Khozikov, "Design considerations of submersible unprotected solid-rotor induction motor," *18th Int. Conf. Electrical Machines*, pp. 1-4, 2008.
[35] A. H. Bonnett and G. C. Soukup, "Rotor failures in squirrel cage induction motors," *IEEE Trans. Ind. Appl.*, Vol. 22, No. 6, pp. 1165-1173, Nov./Dec.1986.
[36] J. H. Jung and B. H. Kown, "Corrosion model of a rotor-bar-under-fault progress in induction motors," *IEEE Trans. Ind. Electron.*, Vol. 53, No. 6, pp. 1829-1841, Dec. 2006.

Jee-Hoon Jung was born in Suwon, Korea, in 1977. He received his B.S., M.S., and Ph.D. degrees from the Department of Electronic and Electrical Engineering, Pohang University of Science and Technology (POSTECH), Pohang, Korea, in 2000, 2002, and 2006, respectively. He was a Senior Research Engineer in the Digital Printing Division of Samsung Electronics Co., Ltd., Suwon, Korea from 2006 to 2009. He was also a Postdoctoral Research Associate in the Electrical and Computer Engineering Department of Texas A&M University at Qatar (TAMUQ), Doha, Qatar from 2009 to 2010. He is currently a Senior Researcher in New & Renewable Energy System Research Center, Smart Grid Research Division of Korea Electrotechnology Research Institute (KERI), Changwon, Korea. His research interests include dc-dc converters, switched mode power supplies, motor drives and diagnosis systems, digital control and signal processing algorithms, digitally controlled power electronics, and power conversions for renewable energy. Recently, he is researching on real-time and power hardware-in-the-loop (PHIL) simulations of the renewable energy sources. Dr. Jung is a member of the IEEE Industrial Electronics Society, IEEE Power Electronics Society, and the Korean Institute of Power Electronics (KIPE).